RESEARCH ARTICLE

NANO · MICRO small
www.small-journal.com

Non-Classical Self-Assembly of Anisotropic Magneto-Organosilica Janus Particles Possessing Surfactant Properties and the Field-Triggered Breakdown of Surface Activity and Amphiphilic Properties

*Cornelia Lanz, Yaşar Krysiak, Xu Liu, Manuel Hohgardt, Peter Jomo Walla, and Sebastian Polarz**

Using colloidal particles as models to understand processes on a smaller scale is a precious approach. Compared to molecules, particles are less defined, but their architecture can be more complex and so is their long-range interaction. One can observe phenomena that are unknown or much more difficult to realize on the molecular level. The current paper focuses on particle-based surfactants and reports on numerous unexpected properties. The main goal is creating an amphiphilic system with responsiveness in surface activity and associated self-organization phenomena depending on applying an external trigger, preferably a physical field. A key step is the creation of a Janus-type particle characterized by two types of dipoles (electric and magnetic) which geometrically stand orthogonal to each other. In a field, one can control which contribution and direction dominate the interparticle interactions. As a result, one can drastically change the system's properties. The features of ferrite-core organosilica-shell particles with grain-like morphology modified by click chemistry are studied in response to spatially isotropic and anisotropic triggers. A highly unusual aggregation–dissolution–reaggregation sequence w as discovered. Using a magnetic field, one can even switch off the amphiphilic properties and use this for the field-triggered breaking of multiphase systems such as emulsions.

1. Introduction

One fascinating application of colloidal particles as models is understanding processes on a different length scale. Current activities to understand emergent phenomena in swarming behavior with the help of so-called active colloids represent an excellent example.[1,2] An active colloid exhibits some motion when an external stimulus, such as a magnetic field (B), is applied, and thus, energy is provided, driving the system.[3–5] An immense potential lies in developing active colloids with smart properties. There are two states, each with a distinct set of properties, and one can switch back and forth. There are two alternatives for the functionalities associated with these states. Either they are in line, complement each other, or can even lead to synergistic effects, or the features may oppose each other. The latter case is exciting because, at certain conditions, one function dominates, enabling a switching/breakdown of the previous state. Li et al. have reported one of the very few cases in the literature.[6] The authors combined sonic-active Au-rods with magneto-active Ni-coated Pd structures. Depending on whether an acoustic or magnetic field is applied, the aggregated or isolated particle state prevails.

An elegant way to implement different functionalities in one particle is the preparation of so-called Janus structures.[7,8] A classical Janus particle comprises two hemispheres with chemically different characteristics.[9–11] Special synthetic strategies are needed to realize such a symmetry-broken architecture.[12] It can be differentiated between compartmentalization and anisotropic surface functionalization methods. Microfluidic techniques are often used for compartmentalization processes to combine two different materials in one particle.[13,14] In turn, for anisotropic surface functionalization, it is pivotal to restrict the accessibility of one particle hemisphere for the reaction.[15,16] Introducing hydrophobic and hydrophilic entities in a Janus architecture leads to particle-based amphiphiles.[10,17]

C. Lanz, Y. Krysiak, S. Polarz
Institute of Inorganic Chemistry
Leibniz Universität Hannover
Callinstrasse 9, D-30167 Hannover, Germany
E-mail: sebastian.polarz@aca.uni-hannover.de
X. Liu, M. Hohgardt, P. J. Walla
Institute of Physical and Theoretical Chemistry
Technische Universität Braunschweig
Hagenring 30, D-38106 Braunschweig, Germany

The ORCID identification number(s) for the author(s) of this article can be found under https://doi.org/10.1002/smll.202304380

DOI: 10.1002/smll.202304380

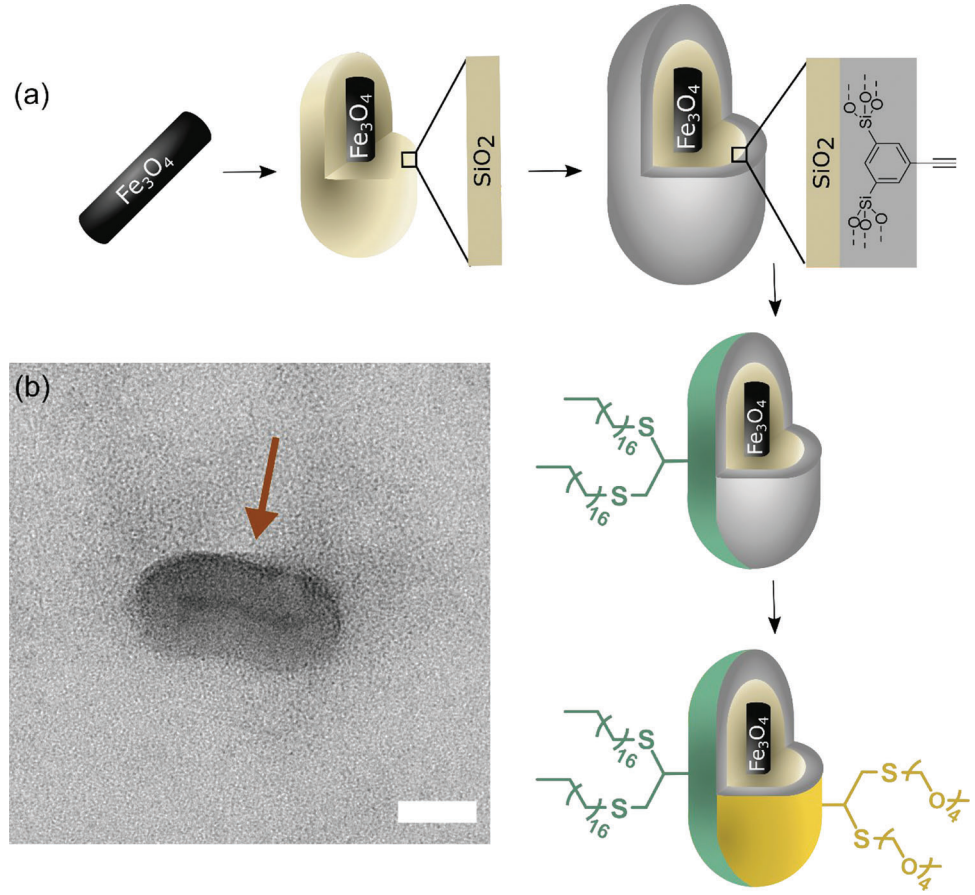

Figure 1. a) Schematic depiction of JAN-rod synthesis. The first steps show material synthesis and further thiol-yne click reaction to obtain amphiphilic functionalization. b) TEM image of JAN-C11COOZn-rod; red arrow shows anisotropic functionalization by a higher contrast due to staining with Zn, scalebar 30 nm.

The concept of the current paper is to equip a particle with Janus architecture with active properties so that an external trigger can switch on and off amphiphilicity and surface activity as a key function. This goal should be realized by particles in which two different vectorial properties are positioned to each other in a fixed, orthogonal orientation. One vectorial property is the difference in polarity or solvent compatibility and is, thus, responsible for the amphiphilic character of the particles. The other property is a magnetic momentum oriented to the electrical dipole at a 90° angle. Because such colloids will orient parallel to a B-field of sufficient strength, we expect noticeable consequences for the amphiphilic properties. The mentioned ideas align with a report by Gao et al., who showed in theoretical work that the control over orientation in a Janus particle system will drastically change the entire set of surface chemistry.[18]

2. Results and Discussion

2.1. Synthesis and Characterization of Janus Colloids with Rod-Shape

In a previous publication, we learned how to prepare colloids with a Janus structure consisting of a spherical magnetite core and an organosilica shell modified asymmetrically by spatially localized click-chemistry.[19] The disadvantage of the latter system is that the magnetic moment in a spherical magnetite crystal is weakly coupled along the easy axis [111] and exhibits relatively free spatial rotation.[20,21] Therefore, it was impossible to position the chemical Janus feature with respect to the magnetic dipole moment. According to multiple literature reports, the magnetic moment's direction in magnetite nanoparticles is much more strongly coupled to the growth direction for an anisotropic crystal shape, particularly for a nanorod morphology.[22–26]

The preparation of the nanorod-based amphiphiles begins with the synthesis of magnetite nanocrystals following a protocol reported by Sun et al.[27] The size and quality of the nanorods have been checked by different methods, including transmission electron microscopy (TEM) analysis (d_{length} = 22.6 nm, $\text{PDI}_{\text{length}}$ = 17.5%, d_{width} = 4.6 nm, $\text{PDI}_{\text{width}}$ = 22.8%), powder X-ray diffraction (PXRD), X-ray photoelectron spectroscopy (XPS), infrared (IR) spectroscopy, and superconducting quantum interference device measurements (SQUID). The data are summarized in Figure S1, Supporting Information. Next, the ferrite nanocrystals can be covered with a shell of pure silica using sol–gel methodology;[28] see **Figure 1**a.

The second shell consists of an organosilica material containing alkyne groups ready for click chemistry modification via the photo-induced thiol-yne reaction.[29] These chemically

isotropic particles with rod-shape (ISO-YNE-rod) were characterized by TEM, energy-dispersive X-ray spectroscopy (EDX), IR, and SQUID as shown in Figure S2, Supporting Information, and represent the starting point for different ways of surface modification. One possibility is the isotropic modification using 1-mercaptoundecanoic acid followed by staining with Zn^{2+} ions (ISO-C_{11}COOZn-rod); see Figure S3, Supporting Information.

The preparation of the Janus particles by anisotropic click modification is much more challenging and is shown in more detail in Figure S4, Supporting Information. The ISO-YNE-rods were assembled into densely packed monolayers on a zinc oxide (ZnO) sputtered silicon wafer. Only the upward side of the particles gets modified by the click reaction by placing the UV light directly from the top. The particles can easily be removed from the surface by dissolving the ZnO layer. After staining (JAN-C_{11}COOZn-rod), one can see an increased TEM image contrast on one hemisphere showing that the anisotropic surface modification was successful (Figure 1b). Because the second "hemisphere" of the particles still contains the unreacted alkyne groups, one can finally introduce a second functionality with different solvophilicity. We present here amphiphilic Janus colloids with rod shape. Octadecyl groups define the hydrophobic side of the particles. Regarding the hydrophilic part, we are focusing on a water-soluble functionality, tetra-ethylene glycol (TEG, see Figure 1a). As a fluorescence active reference, the water-soluble organic dye ATTO 488 is clicked instead of TEG. This dye is frequently used in fluorescence microscopy studies. The resulting colloids are named JAN-C_{18}TEG-rod and JAN-C_{18}ATT-rod, respectively. The chemical characterization of the two systems is summarized in Figure S5, Supporting Information.

2.2. Amphiphilic Self-Assembly

Next, we investigated the aggregation behavior of JAN-rods in a selective solvent such as water. Because molecular surfactants build micelles at a critical micelle concentration (CMC), similar behavior is expected for an aqueous dispersion of JAN-C_{18}ATT-rods, assuming it has amphiphilic properties. The system was investigated by dynamic light scattering (DLS, see **Figure 2**a). At low concentration and room temperature (RT), the data indicate the presence of a species with $d_h \approx 100$ nm, which is almost identical to the size of the non-amphiphilic ISO-YNE-rod determined by DLS (see Figure S6, Supporting Information). Thus, we conclude that the species correlate to isolated particles.

Above $c = 5 \times 10^7$ particles per mL aggregation occurs. Figure 2b shows a representative TEM micrograph of such aggregates. The aggregation of JAN-rods can be explained by a preferential interaction of the nonpolar domains of the particles with each other, with the polar domains oriented to the solvent. However, one must consider that the particle-based amphiphiles' geometry differs significantly from molecular surfactants. The particles resemble a rice grain, and the dipole moment is perpendicular to the long axis of the amphiphile (Figure 1), opposite to the way one finds for surfactants. Unlike a surfactant molecule, the amphiphilic JAN-rods always have a certain polydispersity. The formation of a particle-based analog of a well-defined micelle is hardly possible. In agreement, we find no particular morphology of the aggregates, which also vary in size. The aggregation numbers are small compared to classical micelles.

Because of the unique geometry of the particle-based amphiphiles, we can expect other distinct features of self-assembly. The first unusual feature is observed as dependent on temperature. At higher concentrations (1.4 and 2.4×10^8 particles per mL), a rise in temperature to $T = 40$ °C leads to a dissolution of the aggregates into isolated particles independent of the concentration (Figure 2a,c,d). As this effect is induced by ΔT of only 15 K, we assume the attractive inter-particle interaction is weak.

Surprisingly, for JAN-rods (JAN-C_{18}TEG-rod and also JAN-C_{18}ATT-rod), reaggregation occurs at even higher temperatures ($T = 60$ °C; see Figure 2c; Figures S6,S7, Supporting Information**)**.

Since the described reaggregation effect due to temperature increase is quite unusual, and DLS has the disadvantage that the scattering intensity is dominated by the larger particles present, we wanted to confirm our findings by independent analytical methods. The advantage of the fluorescence active reference system JAN-C_{18}ATT-rod is that it can be used for fluorescence fluctuation spectroscopy (FFS). Compared to DLS, it has a better resolution, so it is possible to detect species of different sizes next to each other in the FFS. The diffusion coefficient can be calculated from the autocorrelation functions of the recorded data. Further evaluation of the hydrodynamic diameter (d_h) can be determined by the Stokes–Einstein equation (see Figure S8, Supporting Information, for more detailed information and concentration-dependent FFS). Figure 2e shows the size distribution function derived from FFS measurements at $T = 25$, 40, and 60 °C. For low temperatures ($T = 25$ °C), two maxima are seen at $d_{h,max} = 80$ and 268 nm. The presence of two species can be explained by an equilibrium between JAN-C_{18}ATT-rod isolated particles and their aggregates. There is a change at $T = 40$ °C. The isolated particle species ($d_{h,max} = 83$ nm) are dominant and larger species are almost absent. It comes to a reaggregation process at $T = 60$ °C as one can only see aggregates with $d_{h,max} > 100$ nm. As a third method to confirm the aggregation–dissolution–reaggregation feature TEM was employed (see Figures S6b,S7b, Supporting Information).

Further experiments were performed to prove that the described behavior is a feature of the amphiphilic nature of the particles combined with the anisotropic shape. The non-amphiphilic ISO-C_{18}-rods show no temperature-dependent de-/reaggregation as shown in Figure S9, Supporting Information. Spherical particles, JAN-C_{18}TEG-sph, also display no particular temperature-dependent behavior (see Figure S10, Supporting Information). The unusual behavior of JAN-rod amphiphiles at higher concentrations (1.4 and 2.4×10^8 particles per mL) shown in Figure 2d is confirmed.

For understanding why reaggregation occurs above 40 °C, referring to molecular amphiphiles might help. The so-called hydrophobic effect is considered a driving force for forming, for example, micelles of molecular surfactants.[30] The hydrophobic effect, in essence, is an entropic phenomenon. The hydrophobic part is surrounded by a shell of entropically unfavorable water molecules, which become released due to the alkyl–alkyl contacts in a micelle. This process leads to an overall entropy gain.

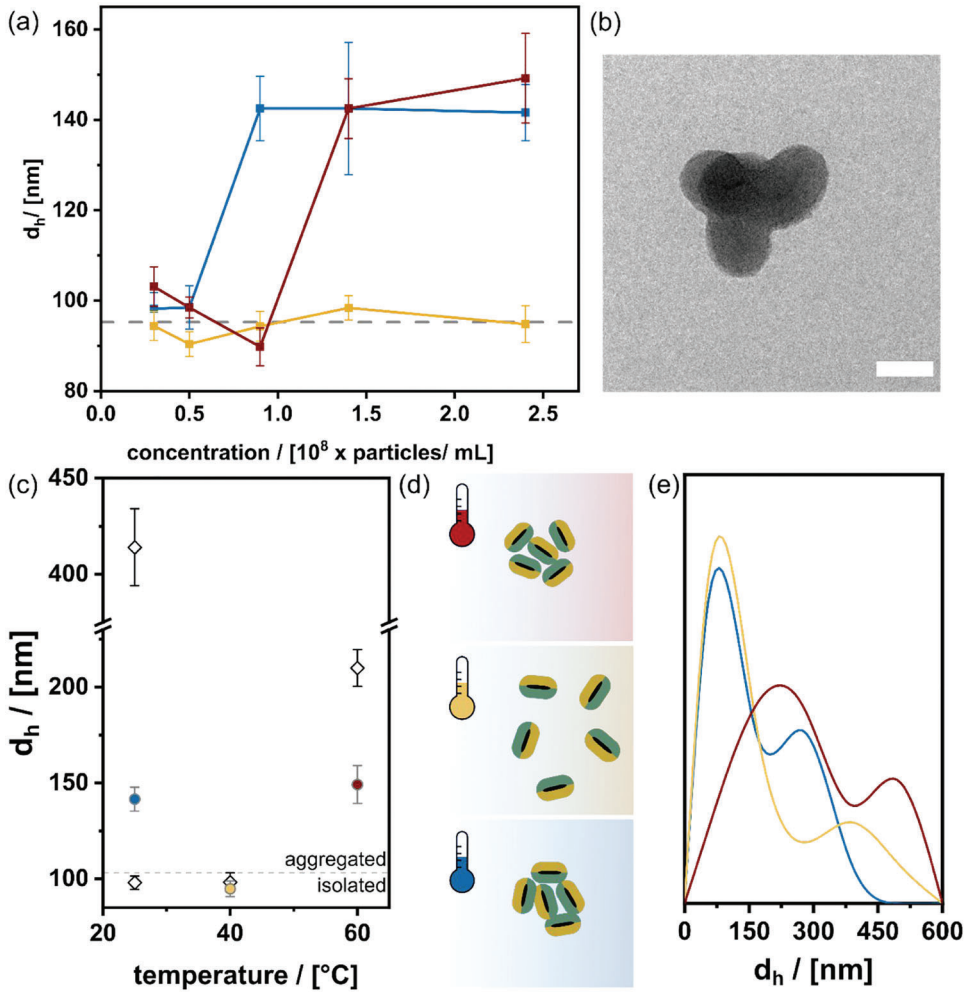

Figure 2. a) Position of the maximum of the particle size distributions obtained from DLS measurement of JAN-C18ATT-Rod in water at different concentrations and temperatures (25 °C = blue; 40 °C = orange; 60 °C = red). Error bars refer to peak width at half height of DLS measurement. The gray dotted line shows the hydrodynamic diameter of ISO-YNE-Rod particles as a reference. b) TEM micrograph of JAN-C18TEG-rod at $c >$ cmc; scalebar 50 nm. c) Position of the maximum of particle size distributions obtained from DLS measurements of JAN-C18TEG-rod (black rhombs) and JAN-C18ATT-rod in water at different temperatures (gray circles, fillings correspond to (d,e); error bars refer to peak width at half height of DLS measurements. The gray dotted line shows the threshold between the isolated and aggregated particle species. d) Schematic depiction of temperature-dependent JAN-rod behavior: aggregation, dissolution, and reaggregation with increasing temperature. e) Temperature-dependent values for dh calculated from FFS data of JAN-C18ATT-rods (blue: 25 °C, orange: 40 °C, red: 60 °C).

Because the entropy term in the Gibbs free enthalpy for the formation of the aggregates is temperature dependent, there might be an explanation for the amphiphilic JAN-rod particles starting to aggregate again at higher temperatures.

The properties of JAN-rod amphiphiles become even more astonishing when one considers the concentration-dependency at $T = 60$ °C. Unlike $T = 25$ °C, the system is already aggregated (at least partially) at $c = 3 \times 10^7$ particles per mL (Figure 2a). These aggregates dissolve when raising the concentration, which is very unusual and counterintuitive. At even higher concentrations, reaggregation occurs for $c > 1 \times 10^8$ particles per mL.

We found bare examples in the literature that describe a concentration-dependent aggregation–dissolution–reaggregation sequence. Reports exist on a phenomenon called depletion flocculation, respectively depletion destabilization.[31,32] Colloidal particles (SiO_2) are stabilized by polymeric agents, for example, poly(vinyl alcohol). At low polymer concentrations, one finds aggregates because of bridging flocculation. The polymer concentration increases, leading to steric stabilization, and the aggregates dissolve. At even higher concentrations, reaggregation takes place because of depletion flocculation. JAN-rods are amphiphiles and particles at the same time. Therefore, one can think of depletion flocculation as an important factor here, too. However, we realize that the explanation is presumably not that simple. Other Janus-type colloids exist in the literature, and also our spherical particles do not exhibit the same phenomena. We can conclude that the anisotropic shape of the particles is a key factor, and magnetic interactions between the particles are additional candidates for influencing the aggregation behavior. This phenomenon requires further experimental and theoretical investigations until a reliable mechanism can be proposed.

2.3. Magnetic Control over Surface Activity

Up to now, the superparamagnetic magnetite core's only role was to control the organosilica nanoparticles' shape. Therefore, we must investigate how the particle-based surfactants react to applying an external magnetic field. To get a first impression of the behavior of the JAN-rod particles at the interface, surface tension is measured by the pendant drop method (see Figure S11, Supporting Information). Compared to pure water, the surface tension is significantly reduced for JAN-rod, which meets the amphiphilic behavior of the particles. An increase in surface tension is observed after placing the magnet beneath the hanging droplet. Interestingly, the influence on surface tension in the external B-field is more pronounced for JAN-rods than for JAN-sph. These results indicate the importance of the shape anisotropy and the precise positioning of the magnetic moment with regard to the amphiphilicity.

For obtaining deeper insights, we have also performed sessile drop measurements in which the magnet field attracts toward an additional interface dependent on the particle shape.

According to Young's equation, the interfacial energy between the liquid and gas phases enters the contact angle of a droplet on a solid surface. The contact angle is, in general, defined as $\cos\theta = (\gamma_{SG}-\gamma_{LS})/\gamma_{LG}$ with γ the surface tensions of the solid–gas (SG), liquid–solid (LS), and the liquid–gas (LG) interface. A droplet of pure water (as a reference) placed on a glass substrate leads to a contact angle of $\theta_{water} = 64°$. See also Figure S12, Supporting Information, for a comparison of contact angle measurements for different concentrations of JAN-rods. In the absence of a magnetic field, there is a qualitative agreement to the behavior of classical amphiphiles meaning that the interfacial energy decreases the higher the amphiphile concentration is. However, because of the complex concentration dependency described in the previous paragraph, one has to be aware not to overinterpret the data. **Figure 3**a shows a contact angle measurement of a sessile drop containing JAN-C_{18}TEG-rod at high concentrations (see Section 2.2). The contact angle is lowered to $\theta = 50°$ ($\Delta\theta$(in %) = −22, referenced to θ_{water}). Amphiphilic species like, JAN-C_{18}TEG-sph,[19] and more specifically JAN-C_{18}TEG-rods, are expected to locate at the air–water interface with the polar parts pointing toward the aqueous phase and the hydrophobic regions pointing toward the gas phase (see Figure 3c). If the concentration of the particles is high, this process lowers the energy of the LG interface clearly, and consequently θ is reduced.

Next, a weak homogeneous magnetic field (300 mT) is applied perpendicular to the substrate. One observes an unexpected substantial rise of the contact angle ($\theta = 72°$, $\Delta\theta$(in %) = +15, referenced to θ_{water}) compared to the measurement without external magnetic field and consequently partial de-wetting of the surface within seconds. A hypothesis for explaining the latter phenomenon is given in Figure 3d. The external magnetic force creates a torque leading to an intermediate state by the orientation of the ferrimagnetic cores parallel to the field (see Figure 3d(I)). The particles feature two directly perpendicular and interdependent vectors/dipoles. One describes the Janus functionalization (electric dipole), the particles' dipolar character, and the other defines the particles' orientation in the *B*-field (magnetic dipole).

A rotation of the particles within the field leads to a misalignment of the amphiphilic particles at the interface. As a result, the energy of the interface rises, which is observed as an increase in θ. If the idea of a magnetic field-induced change of the degree in amphiphilicity is correct, the strength of the magnetic field should matter. The resulting data are shown in Figure 3b with $\Delta\theta$(in %) referenced to pure water on the *y*-axis. The observed S-shape nicely reflects the expected polarization behavior of an ensemble of superparamagnetic particles in an external magnetic field (see Figure 3d). When the field is weak (here <50 mT), the interfacial forces and thermal fluctuations of the magnetic dipole antagonize the reorientation of the amphiphilic particles. Above a certain threshold, when the magnetic field is sufficient, (≈100 mT) rotation of the particles in the field occurs, and the contact angle increases gradually. Although the magnetic field strength decreases exponentially with increasing distance between the magnetic source and the particles, only a weak *B*-field is needed. The amphiphilic properties break apart and the magnetic feature gets dominant. At $B \approx 150$ mT, all particles seem to be oriented parallel to the field, and no further change of θ takes place.

Finally, after the breakdown of the surface activity, more specifically at a more prolonged duration of the magnetic field, the particle's ability for the population of the entire droplet's surface should be reduced. The particles will be dragged down by the *B*-field as shown schematically in Figure 3d(II),e, thereby increasing the energy between the solid–liquid interface. For analyzing this interface, a droplet containing the JAN-rod particle dispersion is placed on a glass slide and taken off with a filter paper after 1 min without and after applying a magnetic field. In its amphiphilic state at $B = 0$ T, where the particles stay at the liquid–air interface, one can see in Figure 3f that JAN-C_{18}TEG-rod was thoroughly removed with the droplet, and no particles are left on the substrate. The situation is different after applying a magnetic field (Figure 3g). One sees that JAN-rod particles are enriched at the three-phase contact line and distributed on the substrate (see Figure S13b, Supporting Information).

Again we want to secure that the observed features are characteristic of the amphiphilic particles with rod-shape, which is why analogous experiments were performed using the non-amphiphilic ISO-rod systems and the spherical, but amphiphilic JAN-sph[19] system as references. A measurement with ISO-C_{18}-rod leads to a contact angle of 63° in zero field and 62° in the presence of the B-field, which is almost identical to the value of pure water (64°); see Figures S12,S14, Supporting Information. As expected, there is reduced surface activity and limited reaction to the magnetic field of ISO-rod particles. The behavior of JAN-C_{18}TEG-sph as a second reference system is shown in Figures S13,S15, Supporting Information. The presence of JAN-C_{18}TEG-sph leads to a substantial reduction of $\theta = 45°$ ($\Delta\theta$(in%) = −30, referenced to θ_{water}) which indicates that amphiphilic properties are present. However, when this system is exposed to a magnetic field, there is an adverse effect compared to JAN-rods. The contact angle is reduced ($\theta = 40°$). The significant difference between the rod- and the spherical-shaped particles is that the relative orientation of the magnetic dipole to the dipolar Janus modification in the case of the spheres is random,[19] and the magnetic moment can move relatively freely in an isotropic-extended crystal (see Figure S15, Supporting Information). Therefore, the most stable configuration of the system is one with the magnetic dipoles oriented parallel

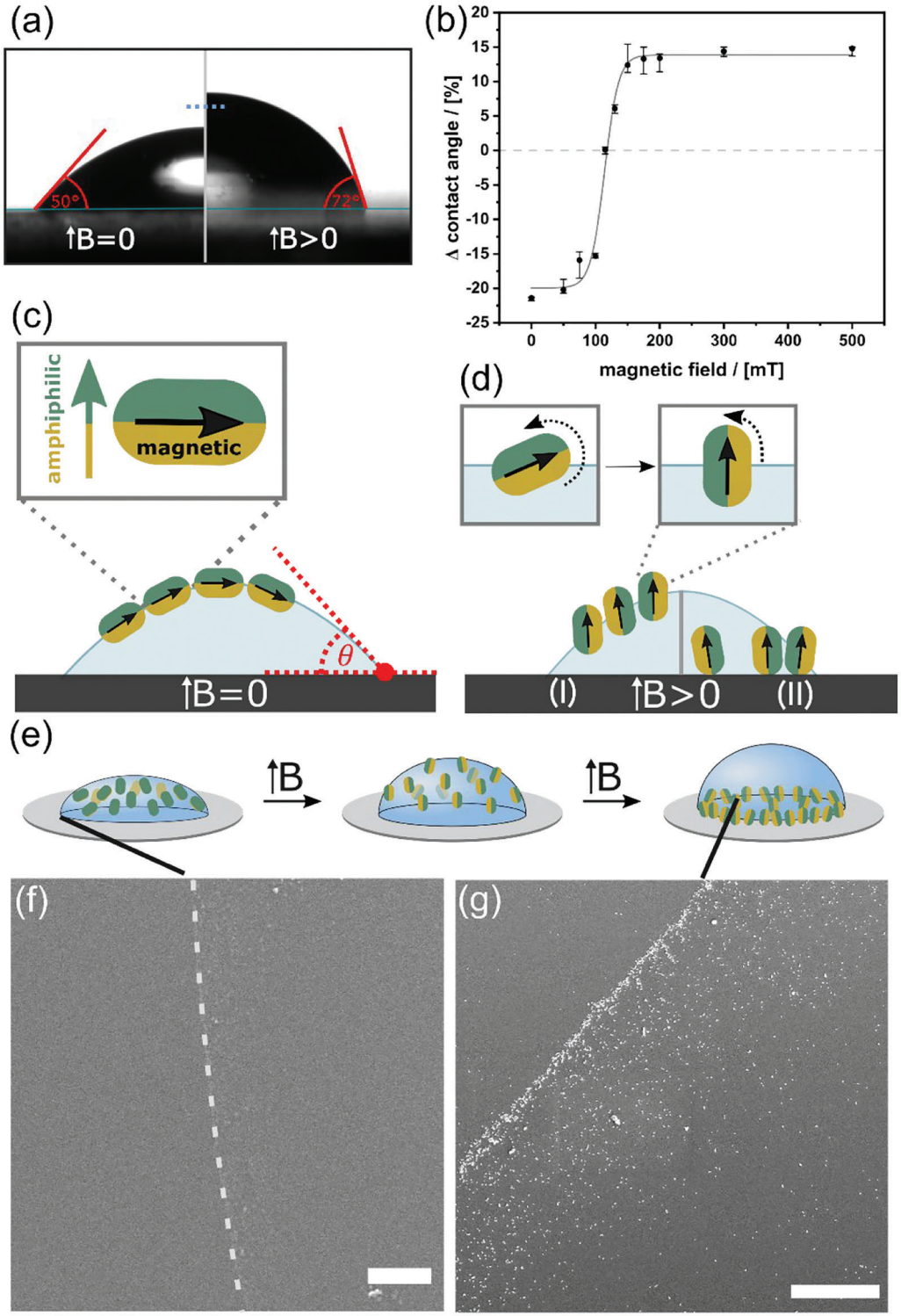

Figure 3. a) Contact angle measurement of a water droplet containing JAN-C18TEG-rod in the absence (left) and after applying an external magnetic field (right). The blue dotted line shows the height of a pure water droplet (as a reference). b) Change in contact angle (in %) of JAN-C18TEG-rods depending on the magnetic field, normalized to contact angle of water, fit in gray. c) Scheme of stabilizing the water–air interface by amphiphilic JAN-C18TEG-rods and resulting contact angle (θ), three-phase-point (red). d) Scheme of the proposed reaction of JAN-C18TEG-rods to an external magnetic field with intermediate state (I) and final state (II). e) Schematic representation of the magnetic-field induced depopulation of JAN-C18TEG-rod from the liquid-gas interface. SEM image taken at the three-phase contact line of a water droplet stabilized by JAN-C18TEG-rod f) before and g) after application of the magnetic field; scalebar 10 µm.

to the B-field and the electrical dipoles still aligned with the interface. By the negative value of $\Delta\theta$, the magnetic fields seem to improve the amphiphilic positioning of the spherical particles at the air–water interface. The spherical particles remain at the liquid–gas interface after applying the magnetic field, and there is no significant change in the energy between the liquid–solid interface (see Figure S13c,d, Supporting Information). This observation also explains the result in pendant drop measurements considering the changed situation regarding the behavior of the hanging drop in the external B-field (see Figure S11, Supporting Information). Here, the JAN-rod particles rotate, which increases the surface tension, and afterward, the particles can translate toward the magnet, which results in a further increase. In comparison, the JAN-sph remains with its amphiphilic state at the interface and only translates toward the magnet, which is why there is a lower increase in surface tension.

In conclusion, the change of the interfacial energy in the JAN-rod/ water system in the presence of a magnetic field is a consequence of two processes: I) the alignment of the particles parallel to the magnetic field reducing the amphiphilic character and II) the depopulation of the particles from the interface. Both processes occur parallel, but the following arguments indicate that the first step is initiating the phenomenon. The first important argument is that the strength of the applied magnetic field is insufficient to drag JAN-sph and ISO-rod to the substrate. Therefore, we assume this factor is the same for JAN-rod fixed even stronger than the water–air interface. However, if the particles rotate first and the amphiphilic character changes, one can explain the experimental findings. The magnetic polarization of the magnetite domain is a very fast process and takes less time than the translation of the entire nanoparticle mass along the droplet's surface. During the fluorescence microscopy measurements, we have also seen that the translation of the particles in the magnetic field is too slow to explain the reaction of the droplet. Final proof for the magnetically-induced change of amphiphilicity will be given in the next section on changing the emulsification properties in an external magnetic field.

Observing the change in the surface tension γ with a high temporal resolution would be exciting. Then, one could resolve the effect solely by process (I). However, we are not aware that such a method exists. We conclude that the presented data for θ and γ always include process (II). As discussed above, process (II) delivers a depopulated air–water interface and a modified solid–liquid interface due to the positioning of the amphiphilic particles.

2.4. Magnetic Breaking of Emulsions

It is an interesting question if the magnetically triggered breakdown of amphiphilic character and surface activity can be transferred to other interfaces, such as liquid–liquid, one finds in emulsions. We present here a first proof-of-concept experiment. JAN-C_{18}TEG-rod was applied as an emulsification agent in a water/toluene mixture. The resulting emulsion was investigated by light microscopy (**Figure 4**a).

The effects can be seen with the bare eye (see Figure S16, Supporting Information; the toluene phase is marked using the water-insoluble dye Nile Red). The as-prepared toluene in water emulsion is built up by small droplets with a diameter below 20 µm. By using the magnetic field (<300 mT) as an external trigger, a marked change can be observed (see Figure 4b). A statistical analysis (see Figure 4d) has been done by counting the emulsion droplets from microscopy images before ($counts_{(B=0)} = 610$, $counts_{(B>0)} = 40$ in 400 × 400 µm area) and after ($d_{(B=0,max)} = 35$ µm, $d_{(B>0,max)} = 120$ µm) placing the emulsion in an external magnetic field. The size of the oil droplets has become much larger, indicating a much more inefficient stabilization of the liquid–liquid interface by JAN-rod. This observation can be explained by the impact of the external magnetic field on the amphiphilic state of the JAN-rods and a starting rotation process due to the interdependent magnetic and electric dipole within the particles. It is well known from emulsion chemistry that the interfacial activity of a surfactant is a crucial factor influencing the size of the oil in water droplets. The less amphiphilic the emulsifier is, the larger and the more unstable the droplets. Because we have seen that the magnetically-induced disorientation influences the amphiphilic properties, the reaction of the emulsion can be understood. However, we see that the strength of the weak magnetic field applied here (<300 mT) is insufficient to break the emulsion. We have learned that an entropic effect by increasing the temperature affects the aggregation state of JAN-rod (see also Figure S16, Supporting Information). Therefore, we repeated the experiment in the external field and at $T = 40$ °C in combination (see Figure 4c; Figure S16, Supporting Information). This time, one observes a synergistic effect by macroscopic phase separation, meaning a quantitative emulsion breakage. The input of the entropic effect and particle rotation is needed to break the amphiphilic property of stabilizing emulsion, leading to phase separation of the water and toluene phase.

3. Conclusion

This work focused on the breakdown of amphiphilic properties in a colloidal amphiphile system triggered by external stimuli. Special rod-shaped nanoparticles with a magnetite core and a Janus-type hydrophobic-hydrophilic shell (JAN-rods) were designed as intrinsically active probes. Hence, the particles exhibit the necessary amphiphilic properties, as they show typical amphiphilic behavior, like the formation of aggregated structures and distinct interfacial activity, and they can act as emulsifiers. Shape anisotropy has been identified as a critical enabler for the influence of amphiphilic properties via external stimuli. As a global external trigger, temperature causes an aggregation–dissolution–reaggregation process, which can be attributed to the hydrophobic effect. An external magnetic field as a local trigger leads to a breakdown of the interfacial activity induced by isolated nanoparticles at the liquid–air interface.

Due to the spatially locked magnetic dipole in the magnetite rods and the interdependency of the electric dipole, particle rotation occurs in magnetic fields. This polarization behavior of the superparamagnetic particles leads to a misalignment of the amphiphilic functionalization at the interface and increasing surface tension. The JAN-rods are also not only influencing the liquid–air interface, but they are also stabilizing liquid–liquid interfaces in an emulsion process. By applying one external trigger each time, the emulsion gets only unstable. Combining both stimuli, the

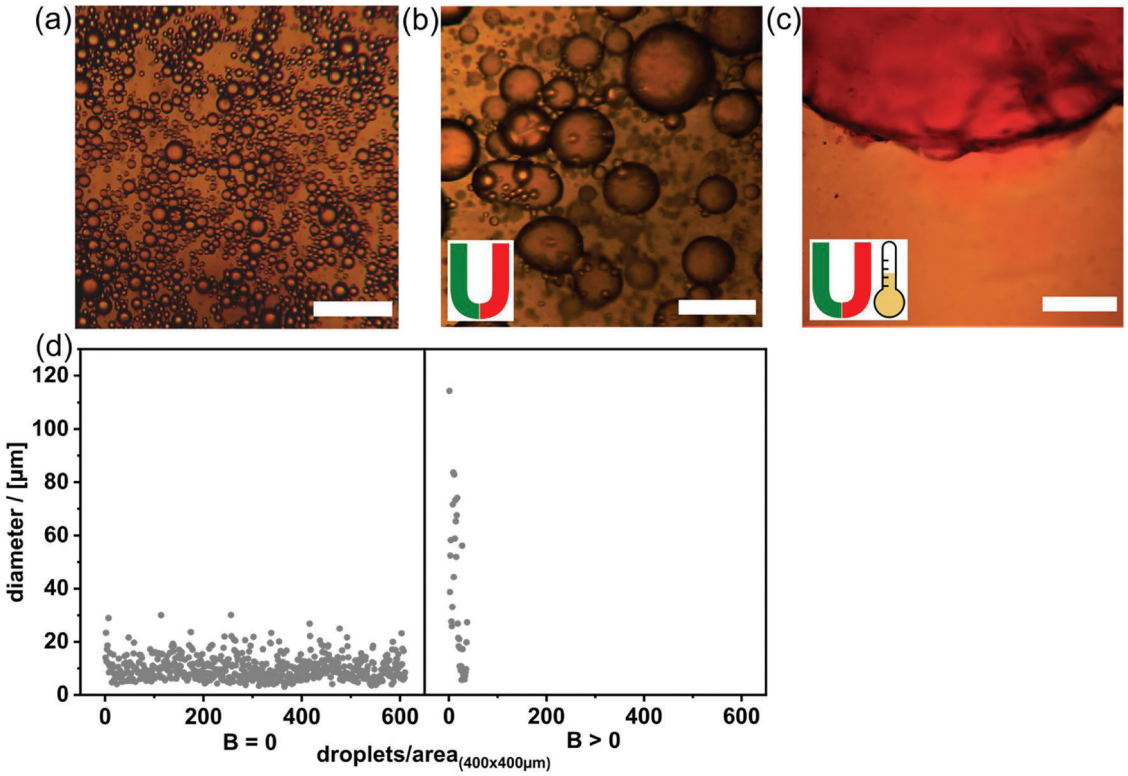

Figure 4. Microscopy images of the oil-in-water emulsion prepared using JAN-C18TEG-rod as the emulsification agent observed a) before, b) after application of a magnetic field, and c) a combination of temperature and magnetic field; scalebar 100 µm. d) Statistic analysis of the droplet size seen in microscopy images (a,b); all droplets in focus level of 400 × 400 µm images are counted and each point corresponds to one droplet.

resulting synergistic effect causes a phase separation. The herein presented study on switchable amphiphilic properties of colloidal amphiphiles can act as a basis for developing intelligent multiphase systems, which can be controlled externally with great precision and, more interestingly, can regulate themselves considering environmental stimuli.

4. Experimental Section

Chemicals were purchased from Sigma-Aldrich and TCI Chemicals. Streptavidin-functionalized ATTO 488 were purchased from ATTO-TEC. Synthesis of ISO-YNE-sphere and 1,3-bistri(isopropoxysilyl)-benzene-5-acetylene were synthesized according to ref. [19].

Synthesis of Magnetite Rods: A solution of 0.8 g hexadecyl amine, 2.0 mL oleic acid, and 8.0 mL 1-octanol was stirred at 55 °C for 30 min. After cooling to RT, 2.0 mL $Fe(CO)_5$ was added to the solution and stirred for 10 min. The reaction solution was filled in a 40.0 mL stainless steel autoclave with teflon inlet and heated to 200 °C for 10 h. The obtained particles were washed three times in ethanol and redispersed in cyclohexane.

Synthesis of ISO-YNE-Rods: In a typical synthesis, 0.5 g Igepal-CO 520 was added to 10.0 mL cyclohexane and sonicated for 15 min before adding 0.5 mL magnetite rods (8.0 mg mL^{-1} in cyclohexane) and 0.9 mL concentrated ammonia. Under vigorous stirring 1.0 mL TEOS were slowly added with 50 µL h^{-1} rate of addition. 5.0 mL methanol were added and the particles were washed three times by centrifugation in ethanol. In a next step, 50.0 mg 1,3-bistri(isopropoxysilyl)-benzene-5-acetylene (UKON-2l) were prehydrolyzed in 1.0 mL *n*-propanol and 50.0 µL, 0.1 M HCl for 2 h. A total of 20 mg particles were dispersed in 120.0 mL ethanol and stirred at 40 °C. The prehydrolyzed UKON-2l was added via a syringe pump with 0.1 mL h^{-1} rate of addition. The obtained particles were washed by centrifugation in ethanol.

Preparation of ISO-C11COOZn-Rods: 125.0 mg mercaptoundecanoic acid and 1.0 mg benzildimethyl acetal (DMPA) were added to 3.0 mg core shell particles in 3.0 mL ethanol in a quartz tube and placed under a UV lamp (365 nm, 100 W) for 10 min. The clicked particles were washed several times by centrifugation in ethanol. Afterward Zn ions were coordinated by addition of 30 mg $Zn(NO_3)_2{\cdot}6H_2O$ to the particle dispersion and heated to 70 °C for 5 min. The resulting ISO-C_{11}COOZn-rods particles were washed by centrifugation in ethanol and redispersed in water.

Preparation of JAN-C11COOZn-Rods: For the monolayer assembly, 100 µL of a 1.0 mg mL^{-1} the ISO-YNE-rod dispersion in ethanol were slowly dried on a 2 × 2 cm Si substrate with a 50 nm amorphous ZnO layer in a covered petri dish. The assembled particles were placed in a petri dish containing a solution of 125.0 mg mercaptoundecanoic acid and 0.5 mg benzildimethyl acetal (DMPA). The UV lamp (365 nm, 100 W) was positioned directly above the petri dish and turned on for 2 min. The obtained particles were removed from the substrate by addition of 150.0 µL 0.01 M HCl and purified by centrifugation in ethanol. Afterward, Zn ions were coordinated by addition of 15.0 mg $Zn(NO_3)_2{\cdot}6H_2O$ to the particle dispersion and heated to 70 °C for 5 min. The resulting JAN-C_{11}COOZn-rods were washed by centrifugation in ethanol and redispersed in water.

Synthesis of 1-Mercapto-3,6,9,12-Tetraoxotridecane (TEG-Thiol): To a solution of triethylen glycol monomethyl ether (20.0 mmol) in 10.0 mL THF, NaOH (36.6 mmol) in 5.0 mL water was added. After degassing for 20 min with N_2 the solution was cooled to 3 °C under vigorous stirring. To the reaction mixture tosyl chloride (20.1 mmol) in 10.0 mL THF was slowly added over 15 min while holding the temperature between 3 and 10 °C. The reaction was heated up to room temperature (RT) and stirred for 12 h. The obtained 1-(*p*-Tolylsulfonyl)−3,6,9-trioxodecane was purified

by extraction with Et_2O and further washing of the organic phase with water. After drying over $MgSO_4$ and removal of the solvent, a yellow oil was obtained.

In the next step, 1-(*p*-Tolylsulfonyl)−3,6,9-trioxodecane (16.3 mmol) and thiourea (16.3 mmol) was dissolved in 10.0 mL ethanol and 7.0 mL water and refluxed for 3 h. A solution of NaOH (18.2 mmol) in 5.0 mL water was added and further refluxed for 1.75 h. The reaction mixture was concentrated to 10 mL, filled up with 5.0 mL water and neutralized with concentrated HCl. Afterward, the product was extracted with chloroform (3 × 5.0 mL), dried over $MgSO_4$ and the solvent was evaporated. For further purification the product was distillated in vacuo (94 °C) and obtained as a colorless liquid. ^{1}H-NMR (400 MHz, $CDCl_3$): δ (ppm) = 1.56 (t, 1H, SH), 2.67 (q, 2H, CH_2), 3.36 (s, 3H, CH_3), 3.56 (m, 10H, CH_2).

Functionalization of ISO-TEG-Rods with 1-Mercapto-3,6,9,12-Tetraoxotridecane (TEG-Thiol): 50 µL TEG-thiol and 1.0 mg benzildimethyl acetal (DMPA) were added to 3.0 mg ISO-YNE-rods in 3.0 mL ethanol in a quartz tube and placed under a UV lamp (365 nm, 100 W) for 10 min. The clicked particles were washed several times by centrifugation in ethanol and redispersed in water.

Functionalization of ISO-C18-Rods with 1-Octadecanethiol: 120 mg 1-octadecanethiol and 1.0 mg benzildimethyl acetal (DMPA) were added to 3.0 mg core shell particles in 3.0 mL toluene in a quartz tube and placed under a UV lamp (365 nm, 100 W) for 10 min. The clicked particles were washed several times by centrifugation with toluene and ethanol and redispersed in water.

Functionalization of JAN-C18TEG-Rods with 1-Octadecanthiol and 1-Mercapto-3,6,9,12-Tetraoxotridecane: For the monolayer assembly, 100 µL of a 1.0 mg mL^{-1} the ISO-YNE-rod dispersion in ethanol were slowly dried on a 2 × 2 cm Si substrate with a 50 nm amorphous ZnO layer in a covered petri dish. The assembled particles were placed in a petri dish containing a solution of 60.0 mg 1-octadecanethiol, 0.5 mg benzildimethyl acetal (DMPA), and 1.0 mL toluene. The UV lamp (365 nm, 100 W) was positioned directly above the petri dish and turned on for 2 min. The substrate was washed with toluene and ethanol two times. To obtain the right amount of particles for further measurements the synthesis was repeated with six substrates. The obtained particles were removed from the substrate by addition of 150.0 µL 0.01 M HCl, and purified by centrifugation in ethanol. Afterward, the particles were dispersed in 1.0 mL ethanol. 50.0 µL TEG-thiol and 0.5 g DMPA were added to the dispersion and placed under a UV lamp (365 nm, 100 W) for 5 min. The clicked particles were washed several times by centrifugation in ethanol and redispersed in water.

Functionalization of JAN-C18ATT-Rods with 1-Octadecanthiol and ATTO 488: Synthesis of Biotin Thiol: 526.0 mg biotin-succinimide, 178.8 mg cysteamine dihydrochloride, and 600.0 µL triethylamine were added to 25.0 mL DMF and stirred for 18 h at room temperature. The white solid was filtrated and dried under high vacuum. HRMS (ESI) *m/z* calculated for $C_{12}H_{21}N_3O_2S_2Na$: 326.0973, found: 326.0968.

Anisotropic Click Reactions: For the monolayer assembly, 100 µL of a 1.0 mg mL^{-1} the core shell particles dispersion in ethanol were slowly dried on a 2 × 2 cm Si substrate with a 50 nm amorphous ZnO layer in a covered petri dish. The assembled particles were placed in a petri dish containing a solution of 20.0 mg Biotin thiol, 0.5 mg benzildimethyl acetal (DMPA), 0.5 mL DMF, and 0.5 mL water. The UV lamp (365 nm, 100 W) was positioned directly above the petri dish and turned on for 2 min. The substrate was washed with water two times. To obtain the right number of particles for further measurements the synthesis was repeated with six substrates. The obtained particles were removed from the substrate by addition of 150.0 µL 0.01 M HCl and purified by centrifugation in ethanol. Afterward, the particles were dispersed in 1.0 mL toluene. 60.0 mg 1-octadecanethiol and 0.5 g DMPA were added to the dispersion and placed under a UV lamp (365 nm, 100 W) for 5 min. The clicked particles were washed several times by centrifugation in ethanol and redispersed in water.

ATTO 488 Functionalization: For binding of streptavidin-functionalized ATTO 488 to the biotin-functionalized hemisphere 50 µL of 2 µL mL^{-1} ATTO 488-streptavidin solution (in water) was added to the clicked particles and stirred for 12 h. Afterward the particles were washed several times in water and redispersed in water.

Preparation of Toluene/Water Emulsion with JAN-C18TEG-Rods: 0.1 mL JAN-C_{18}TEG-rods (1.4×10^8 particles per mL) in water, 50.0 µL toluene and 1.0 mg nile red were put into a 4 mm glass tube and shook for 1 min. After 5 min the microscopy images were taken.

Analytical Methods: NMR spectra were measured with a Bruker Ascend 400 MHz spectrometer. ESI-MS spectrum was recorded with a Micromass LCT Premiere. SEM images were acquired with a Regulus 8230 from Hitachi. TEM images and EDX spectra were obtained with a FEI Tecnai G2 F20 TMP (200 kV). Further TEM images were acquired with a Hitachi HT7800 (120 kV). DLS measurements were acquired with a Malvern Zetasizer ZMV 2000. IR spectra were measured with a Bruker Vertex 70v. NTA measurements were used to calculate the particle concentration (particles per mL) with a Malvern NanoSight LM10. Contact angle measurements were recorded with a dataphysics OCA 15 EC. The used NdFeB magnet (10 × 10 × 3 mm, magnetic field density: 380 mT) was positioned 1 mm from the bottom of the drop. XPS spectrum was measured with a Versaprobe III from Physical Electronis GmbH. The field- and temperature-dependent SQUID measurements have been acquired using a Quantum Design MPMS3 magnetometer. Fluorescence spectra were acquired using an Agilent Cary Eclipse. The microscopy images were obtained using an Olympus CX41RF.

Confocal Fluorescence Microscopy: The confocal fluorescence microscope was used for fluorescence fluctuation detection. The inverted microscope (Olympus, IX73) was established with a water immersion objective (UPLSAPO, 60x, 1.2NA). The excitation laser (Coherent, 488 nm) was guided to the main dichroic mirror (Chroma, 405/488/561/640) and entered the microscope. The emission light was separated with the main dichroic mirror and filtered with a band-pass (Semrock, BP525/40). Then the fluorescence passed through a pinhole with 50 µm and finally focused onto the avalanche photon diode detector (Excelitas Tchnologies, SPCM-AQRH-44-TR). In addition, the microscope stage was attached with an incubator chamber and heater (Zeiss, CO_2 Module S) to control the temperature.

In FFS experiments, 100 µL of sample solution was pipetted onto the microscope coverslip. The exciting laser was focused on the volume or interface of the liquid droplet, respectively.

In this work, autocorrelation functions of the recorded data were calculated off-line, using software ISS VistaVision 4.2. The fitting model was 2D Gaussian in presence of a Triplet state.

$$G(\tau) = \frac{1}{N}\prod_{i=1}^{n}\left(1 + A_i \exp\left(-\frac{\tau}{\tau_i}\right)\right)\frac{1}{\left(1+\frac{\tau}{\tau_D}\right)} \quad (1)$$

where: $\tau_D = \frac{r_0^2}{4D}$ and $A_i = \frac{F_i}{(1-F_i)}$, F is the fraction of molecules residing in the dark state at any time.

To characterize the FFS setup ATTO 488 (1 and 0.1 nM) was used as a calibration standard, from the relation between the translational diffusion time coefficient D and diffusion time τ_D, the horizontal radius of confocal detection volume r_0 can be quantified.[33]

$$D = \frac{r_0^2}{4\tau_D} \quad (2)$$

where D is the temperature-corrected diffusion coefficient for ATTO 488, 3.49×10^{-6} cm^{-6} s^{-1} in water at 20°.[34] The fluorescence time traces of ATTO 488 with two concentrations were recorded three times for 300 s, τ_D were fitted with the autocorrelation function with 2D Triplet Gaussian 1 Species diffusion model (Figure S17, Supporting Information). For ATTO 488, the fits of all six traces yielded a mean diffusion time of 248.8 µs ± 6.6 µs, which was further determined the horizontal radius of confocal detection volume r_0 is 590 ± 8 nm. For the JAN-C_{18}ATT-rod, the fluorescence traces were recorded for 300 s and the autocorrelation function was fitted for each 10 s interval with 2D triplet Gaussian 2 species diffusion model.

The diffusion time can be obtained from the fitted results. With Equation (1) the diffusion coefficient can be further calculated, subsequently, the hydrodynamic radius R_h can be determined from Stocks–Einstein equation (3).[33]

$$R_h = \frac{k_B T}{6\pi\eta D} \tag{3}$$

where k_B is the Boltzmann constant, T is the absolute temperature, η is the temperature-corrected viscosity of the water, η (20°) = 1.0016 mPa s, η (40°) = 0.6527 mPa s, η (60°) = 0.4660 mPa s.[35] For pure ATTO 488 in water at 20°, the R_h is 0.61 nm.

Supporting Information

Supporting Information is available from the Wiley Online Library or from the author.

Acknowledgements

Part of this work was funded by the German Research Foundation (Deutsche Forschungsgemeinschaft, DFG) under Germany's excellence strategy within the cluster of excellence PhoenixD (EXC 2122).

Open access funding enabled and organized by Projekt DEAL.

Conflict of Interest

The authors declare no conflict of interest.

Data Availability Statement

The data that support the findings of this study are available in the supplementary material of this article.

Keywords

active colloids, Janus nanostructures, magnetic surfactants, particle-based materials

Received: May 25, 2023
Revised: July 26, 2023
Published online: August 30, 2023

[1] C. Reichhardt, C. Reichhardt, *Annu. Rev. Condens. Matter Phys.* **2017**, *8*, 51.
[2] D. Jin, L. Zhang, *Acc. Chem. Res.* **2022**, *55*, 98.
[3] A. Zottl, H. Stark, *J. Phys. Condens. Matter* **2016**, *28*, 253001.
[4] S. Ebbens, *Curr. Opin. Colloid Interface Sci.* **2016**, *21*, 14.
[5] J. Deng, M. Molaei, N. Chisholm, T. Yao, A. Read, K. Stebe, *Curr. Opin. Colloid Interface Sci.* **2022**, *61*, 101629.
[6] J. Li, T. Li, T. Xu, M. Kiristi, W. Liu, Z. Wu, J. Wang, *Nano Lett.* **2015**, *15*, 4814.
[7] H. Lv, Y. Xing, X. Du, T. Xu, X. Zhang, *Soft Matter* **2020**, *16*, 4961.
[8] A. Sánchez, K. Ovejero Paredes, J. Ruiz-Cabello, P. Martínez-Ruíz, J. M. Pingarrón, R. Villalonga, M. Filice, *ACS Appl. Mater. Interfaces* **2018**, *10*, 31032.
[9] J. Hu, S. Zhou, Y. Sun, X. Fang, L. Wu, *Chem. Soc. Rev.* **2012**, *41*, 4356.
[10] S. Razavi, L. M. Hernandez, A. Read, W. L. Vargas, I. Kretzschmar, *J. Colloid Interface Sci.* **2020**, *558*, 95.
[11] K. Lee, Y. Yu, *J. Mater. Chem. B* **2017**, *5*, 4410.
[12] A. Kirillova, C. Marschelke, A. Synytska, *ACS Appl. Mater. Interfaces* **2019**, *11*, 9643.
[13] S. Bhaskar, K.-H. Roh, X. Jiang, G. L. Baker, J. Lahann, *Macromol. Rapid Commun.* **2008**, *29*, 1655.
[14] Z. Nie, W. Li, M. Seo, S. Xu, E. Kumacheva, *J. Am. Chem. Soc.* **2006**, *128*, 9408.
[15] L. Hong, S. Jiang, S. Granick, *Langmuir* **2006**, *22*, 9495.
[16] A. Wittmeier, A. Leeth Holterhoff, J. Johnson, J. G. Gibbs, *Langmuir* **2015**, *31*, 10402.
[17] D. Wu, B. P. Binks, A. Honciuc, *Langmuir* **2018**, *34*, 1225.
[18] H.-M. Gao, Z.-Y. Lu, H. Liu, Z.-Y. Sun, L.-J. An, *J. Chem. Phys.* **2014**, *141*, 134907.
[19] C. Lanz, M. Schlötter, N. Klinkenberg, P. Besirske, S. Polarz, *Angew. Chem., Int. Ed.* **2020**, *59*, 8902.
[20] C. Shasha, K. M. Krishnan, *Adv. Mater.* **2021**, *33*, 1904131.
[21] M. Chariaou, L. Rahn-Lee, J. Kind, I. García-Rubio, A. Komeili, A. U. Gehring, *Biophys. J.* **2015**, *108*, 1268.
[22] J. Wang, Z. Peng, Y. Huang, Q. Chen, *J. Cryst. Growth* **2004**, *263*, 616.
[23] Z. Zhou, X. Zhu, D. Wu, Q. Chen, D. Huang, C. Sun, J. Xin, K. Ni, J. Gao, *Chem. Mater.* **2015**, *27*, 3505.
[24] R. Moreno, S. Poyser, D. Meilak, A. Meo, S. Jenkins, V. K. Lazarov, G. Vallejo-Fernandez, S. Majetich, R. F. L. Evans, *Sci. Rep.* **2020**, *10*, 2722.
[25] Y. Yang, X. Liu, Y. Lv, T. S. Herng, X. Xu, W. Xia, T. Zhang, J. Fang, W. Xiao, J. Ding, *Adv. Funct. Mater.* **2015**, *25*, 812.
[26] Z. Xu, Z. Wei, P. He, X. Duan, Z. Yang, Y. Zhou, D. Jia, *Chem. Commun.* **2017**, *53*, 11052.
[27] H. Sun, B. Chen, X. Jiao, Z. Jiang, Z. Qin, D. Chen, *J. Phys. Chem. C* **2012**, *116*, 5476.
[28] H. L. Ding, Y. X. Zhang, S. Wang, J. M. Xu, S. C. Xu, G. H. Li, *Chem. Mater.* **2012**, *24*, 4572.
[29] R. Hoogenboom, *Angew. Chem., Int. Ed.* **2010**, *49*, 3415.
[30] Y. R. Espinosa Silva, J. R. Grigera, *RSC Adv.* **2015**, *5*, 70005.
[31] S. Kim, K. Hyun, J. Y. Moon, C. Clasen, K. H. Ahn, *Langmuir* **2015**, *31*, 1892.
[32] T. Kuroiwa, I. Kobayashi, A. M. Chuah, M. Nakajima, S. Ichikawa, *Adv. Colloid Interface Sci.* **2015**, *226*, 86.
[33] I. V. Perevoshchikova, E. A. Kotova, Y. N. Antonenko, *Biochemistry (Moscow)* **2011**, *76*, 497.
[34] P. Kapusta, *PicoQuant GmbH* **2010**, *2*, 1.
[35] E. R. Likhachev, *Tech. Phys.* **2003**, *48*, 514.